Contents lists available at SciVerse ScienceDirect

Journal of Power Sources

journal homepage: www.elsevier.com/locate/jpowsour

Fe$_3$O$_4$/carbon core–shell nanotubes as promising anode materials for lithium-ion batteries

Hui Xia [a,*], Yunhai Wan [a], Guoliang Yuan [a], Yongsheng Fu [b], Xin Wang [b,**]

[a] School of Materials Science and Engineering, Nanjing University of Science and Technology, Xiaolingwei 200, Nanjing, Jiangsu 210094, China
[b] Key Laboratory of Soft Chemistry and Functional Materials, Nanjing University of Science and Technology, Ministry of Education, Nanjing 210094, China

HIGHLIGHTS

- Fe$_3$O$_4$/carbon core–shell nanotubes have been successfully synthesized.
- The hybrid electrode shows a large reversible capacity up to 938 mAh g^{-1}.
- The hybrid electrode also shows excellent cycling stability and rate capability.

GRAPHICAL ABSTRACT
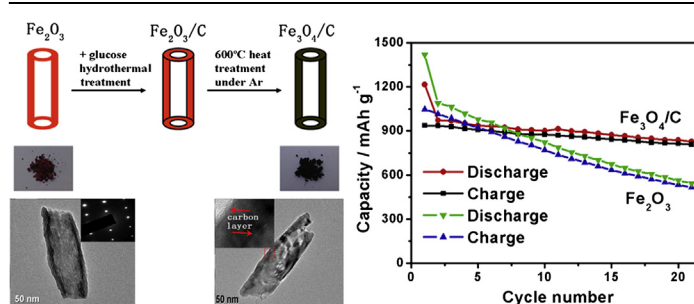
ABSTRACT

Magnetite (Fe$_3$O$_4$)/carbon core–shell nanotubes have been successfully synthesized by partial reduction of monodispersed hematite (Fe$_2$O$_3$) nanotubes with carbon coating. Fe$_2$O$_3$ is completely converted to Fe$_3$O$_4$ during the reduction process and a thin carbon layer is continuously coated on the surface of Fe$_3$O$_4$ with the nanotube morphology reserved. The Fe$_3$O$_4$/carbon core–shell nanotubes exhibit superior electrochemical properties as anode material for lithium-ion batteries compared with the Fe$_2$O$_3$ and Fe$_3$O$_4$ nanotubes. The Fe$_3$O$_4$/carbon core–shell nanotubes electrode shows a large reversible capacity up to 938 mAh g^{-1} as well as improved cycling stability and excellent rate capability. The promising anode performance of the Fe$_3$O$_4$/carbon core–shell nanotubes can be attributed to their tubular morphology and continuous carbon coating, which provide improved structural stability and fast charge transport.

1. Introduction

During the past few decades, rechargeable lithium-ion batteries (LIBs) with high energy density, light weight, long cycle life, and environmental friendliness have been widely used as power sources for various portable electronic devices such as cellular phones, laptop computers, digital cameras and etc [1,2]. More recently, they have attracted growing attention as power supplies for hybrid, plug-in hybrid, and all electric vehicles. To meet the ever increasing demands for larger energy density and power density, intensive research has been invested to develop new electrode materials with improved electrochemical performance. For instance, transition metal oxides such as Fe$_2$O$_3$, Fe$_3$O$_4$, Co$_3$O$_4$, and MnO$_2$ have attracted a

---

* Corresponding author. Tel.: +86 25 84315606; fax: +86 25 84315159.
** Corresponding author. Tel.: +86 25 84305667; fax: +86 25 84315054.
E-mail addresses: xiahui@njust.edu.cn, jasonxiahui@gmail.com (H. Xia), wxin@public1.ptt.js.cn (X. Wang).

lot of interest as anode materials for LIBs due to their higher theoretical capacities than that of commercial graphite anode [3–11]. Among these anode materials, Fe_3O_4 (magnetite) has many advantages in terms of relatively high electronic conductivity, low cost, and environmental benignity, thus has attracted considerable attention [12–14]. However, like other transition metal oxides, Fe_3O_4 still suffers from rapid capacity fading during the cycling process due to the electrode pulverization, which leads to loss of contact between electrode materials and current collectors.

It has been well demonstrated that the cycling stability of Fe_3O_4 could be partially solved in nanostructured electrode materials due to their large surface-to-volume ratio and small dimensions, which can alleviate the mechanical stress associated with Li insertion/extraction [15,16]. By far, various nanostructures of Fe_3O_4, including nanoparticles, nanoflakes, nanorods, and nanobelts, have been synthesized and tested in lithium-ion batteries [17–20]. However, Fe_3O_4 nanotubes, which could be ideal for accommodating large volume changes, have very limited reports for their electrochemical performance as anode materials for LIBs [21]. Although nanotubes of a wide range of materials in various types have been prepared by different strategies, it remains a challenge to synthesize nanotubes of metal oxides with isotropic crystal structure. Nanotubes of various metal oxides are usually prepared by a template method. Previously, Jia, Sun and Yan et al. firstly reported the synthesis of Fe_2O_3 nanotubes by a hydrothermal method [22,23]. Recently, Liu et al. [24] prepared Fe_2O_3 nanotube arrays by a sacrificial template-accelerated hydrolysis approach and Wang et al. [25] prepared polycrystalline Fe_2O_3 nanotubes by one-step template-engaged precipitation of $Fe(OH)_x$ followed by thermal annealing. Both Fe_2O_3 nanotube samples exhibit promising cycling stability as anodes for lithium-ion batteries. Nevertheless, the high surface area of nanostructured electrode materials raises the risk of solid electrolyte interphase (SEI) layer formation, which could cause a high level of irreversibility and poor cycle life [26]. Therefore, surface modification should be considered for nanostructured transition metal oxides as anode materials for LIBs.

Carbon coating is one of the most widely used surface modification techniques and has been used for anode materials as it may serve as perfect barrier to protect inner active material and maintain its high capacity [27–29]. Recently, carbon coated Fe_2O_3 and Fe_3O_4 are extensively studied as anode materials for lithium-ion batteries [27–37]. For example, carbon-decorated single crystalline Fe_3O_4 nanowires [7], Fe_3O_4/carbon core–shell nanorods [15], and carbon coated Fe_3O_4 nanospindles [26], have been prepared to improve the electrochemical performance of the pure Fe_3O_4 electrodes. In this work, Fe_2O_3 nanotubes were synthesized by a simple hydrothermal treatment without using template. A thin carbon layer was coated on the Fe_2O_3 nanotubes by another hydrothermal treatment using glucose. The carbon-coated Fe_2O_3 nanotubes were easily converted to carbon-coated Fe_3O_4 nanotubes by thermal annealing in Ar atmosphere. It was found that the Fe_3O_4/carbon core–shell nanotubes exhibit large reversible capacity (938 mAh g^{-1}), significantly improved cycling stability, and high rate capability compared with the bare Fe_2O_3 and Fe_3O_4 nanotubes.

2. Experimental

2.1. Synthesis of Fe_2O_3 and Fe_3O_4 nanotubes

The Fe_2O_3 nanotubes were synthesized by a simple hydrothermal treatment reported in Fan's work [38]. In a typical synthesis procedure, 0.4320 g $FeCl_3 \cdot 6H_2O$ and 0.0066 g $NH_4H_2PO_4$ were added to 80 mL distilled water with vigorous stirring. After stirring for 10 min, the mixture was transferred into a Teflon-lined stainless-steel autoclave with a capacity of 100 mL. The autoclave was

then put into an electric oven for hydrothermal treatment at 200 °C for 96 h. The autoclave was cooled down to room temperature naturally and the red precipitate was separated by centrifugation, washed with distilled water, and dried under vacuum at 80 °C. The obtained samples were Fe_2O_3 nanotubes. The Fe_3O_4 nanotubes were synthesized according to a previous work [39]. In a typical synthesis procedure, 0.3 g of Fe_2O_3 nanotubes were heated in a horizontal quartz tube furnace at 420 °C for 120 min under a constant flow of 5% H_2/95% Ar at 800 sccm. After that, the furnace was cooled down to room temperature without changing the atmosphere and black Fe_3O_4 product was collected from the small quartz.

2.2. Synthesis of Fe_3O_4/carbon core–shell nanotubes

0.20 g Fe_2O_3 nanotubes were dispersed in 20 mL distilled water by ultrasonication for 1 h to form a suspension. In the next step, 0.31 g glucose ($C_6H_{12}O_6 \cdot 3H_2O$) was dissolved in the above suspension and 5 mL ethanol was added to the suspension with gentle stirring. After stirring for 10 min, the mixed solution was transferred to a 30 mL Teflon-lined autoclave for hydrothermal treatment at 180 °C for 12 h. After the autoclave cooled down to room temperature, the carbon precursor-coated Fe_2O_3 nanotubes were harvested by centrifugation and washed with distilled water, then dried in an electric oven at 80 °C. The resulting sample filled in an alumina crucible was heated at 600 °C in an electric furnace under Ar atmosphere for 6 h for carrying out the carbon-thermal reduction to obtain the final Fe_3O_4/carbon core–shell nanotubes.

2.3. Structural and morphology characterization

The crystallographic information and composition of the products were investigated by X-ray diffraction (XRD, Shimadzu X-ray diffractometer 6000, Cu K_α radiation), Raman spectroscopy (Jobin-Yvon T6400 Micro-Raman system), inductively coupled plasma-optical emission spectroscopy (ICP, Thermo Elemental IRIS 1000), and X-ray photoelectron spectroscopy (XPS, PHI Quantera SXM Scanning X-ray Microprobe). Raman spectroscopy measurements were carried out using a Jobin-Yvon T64000 micro-Raman system equipped with a charge-coupled device detector. XPS analysis was performed on the thin film with a VG ESCALAB MK spectrometer using Al K radiation (1486.6 eV). An analyzer with a pass energy of 20 eV was adopted, and a C 1s peak at 284.6 eV due to adventitious carbon was used as an internal reference. The carbon content of the composite was also characterized by thermogravimetric analysis (TGA, Shimadzu DTG-60H). The morphology and structure of the products were investigated by field emission scanning electron microscopy (FESEM, Hitachi S4300), transmission electron microscopy (TEM, JEOL, JEM-2010) and high resolution transmission electron microscopy (HRTEM).

2.4. Electrochemical measurements

To prepare the working electrodes, slurries were prepared by mixing 80 wt% active material (Fe_2O_3 nanotubes, Fe_3O_4 nanotubes and Fe_3O_4/carbon core–shell nanotubes), 10 wt% acetylene black (Super-P), and 10 wt% polyvinylidene fluoride (PVDF) binder in N-methyl-2-pyrrolidinone (NMP). The slurries were coated on the Cu foils and dried at 120 °C for 2 h to remove the solvent. The dried electrodes were pressed and cut into small disks (10 mm in diameter). The small disks were further dried at 80 °C in a vacuum oven for 12 h before battery tests. Half cells using Li foil as both counter and reference electrodes were assembled with Lab-made Swagelok cells for the electrochemical measurements. 1 M $LiPF_6$ in ethylene carbonate and diethyl carbonate (EC/DEC, $v/v = 1:1$)

solution was used as the electrolyte and Celgard 2400 was used as the separator. Galvanostatic charge and discharge measurements were carried out in the voltage range between 0.01 and 3 V at different current densities using LAND CT2001A electrochemical workstation at room temperature.

3. Results and discussion

The phase purity and crystal structure of the products were investigated by XRD. As shown in Fig. 1b, all of the diffraction peaks can be exclusively indexed to the trigonal α-Fe_2O_3 (JCPDS No. 87-1165), and no other impurities are observed. When the Fe_2O_3 nanotubes were coated with carbon and heated in Ar atmosphere at 600 °C, a phase transition took place in the iron oxide as Fig. 1a shows a completely different XRD pattern. All diffraction peaks in Fig. 1a can be indexed to face centered Fe_3O_4 (JCPDS No. 65-3107). No XRD peaks corresponding to graphite are found in the XRD pattern of the Fe_3O_4/carbon core–shell nanotubes, which indicates the carbon coatings are probably in amorphous state [27]. It is noticed that the XRD pattern of Fe_3O_4 is quite similar to that of γ-Fe_2O_3. The existence of γ-Fe_2O_3 in the products can be ruled out because γ-Fe_2O_3 cannot withstand heat-treatment as it converts to α-Fe_2O_3 at about 400 °C [26]. The XRD pattern of the bare Fe_3O_4 nanotubes obtained from the reduction of Fe_2O_3 nanotubes is exactly the same as that of the Fe_3O_4/carbon nanotubes, which is not shown here.

Raman spectroscopy was further performed to investigate the structure and phase composition of the products. Fig. 2a shows the Raman spectrum of the carbon precursor-coated Fe_2O_3 nanotubes. As hematite belongs to the D_{3d}^6 crystal space group with two A_{1g} modes and five E_g modes, two peaks at 225 and 486 cm^{-1} are assigned to the A_{1g} modes and three peaks at 290, 401, and 597 cm^{-1} are assigned to E_g modes [40]. Another two peaks at 1300 and 1587 cm^{-1} can be assigned to the D and G bands for carbon [41]. The G band, corresponding to the first order scattering of the E_{2g} mode observed for sp^2 domains, is characteristic for graphitic sheets, whereas the D band can be attributed to the presence of sp^3 defects within the carbon [42]. Fig. 2b shows the Raman spectrum of the Fe_3O_4/carbon core–shell nanotubes. A strong peak at 670 cm^{-1} and two small peaks at 538 and 300 cm^{-1} can be assigned to the A_{1g}, T_{2g}, and E_g modes of Fe_3O_4, respectively [40]. Another two peaks at 1335 and 1594 cm^{-1} correspond to the D and G bands for carbon. The intensity ratio of the D and G band (I_D/I_G) is indicative of the degree of graphitization [43]. The ratio value for the Fe_3O_4/carbon core–shell nanotubes is 0.97, whereas it is 1.25 for the carbon precursor-coated Fe_2O_3 nanotubes, which indicates that
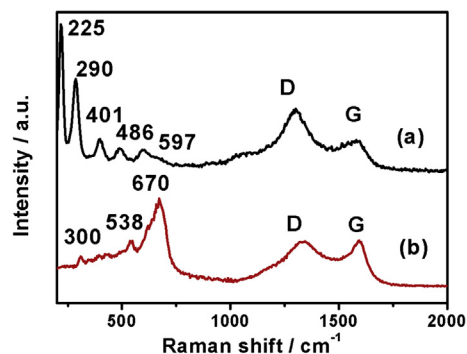

Fig. 2. Raman spectra of (a) the carbon precursor-coated α-Fe_2O_3 nanotubes and (b) the Fe_3O_4/carbon core–shell nanotubes.

the degree of graphitization of the carbon within Fe_3O_4/carbon core–shell nanotubes is strongly enhanced.

The surface morphology and microstructure of the α-Fe_2O_3 nanotubes and the Fe_3O_4/carbon core–shell nanotubes were characterized by FESEM and TEM. Fig. 3a shows the FESEM image of the as-prepared α-Fe_2O_3 nanotubes. It can be seen that large-scale hollow structured Fe_2O_3 nanocrystals with uniform size and tubular morphology have been fabricated by the hydrothermal treatment. The average length of these nanotubes is about 250 nm and the average outer diameter of these nanotubes is about 90 nm. After reduction, the obtain Fe_3O_4 nanotubes preserved the similar morphology as the Fe_2O_3 nanotubes. Fig. 3b shows the FESEM image of the Fe_3O_4/carbon core–shell nanotubes. It can be seen that there is no significant change in morphology, indicating the tubular structure is stable under hydrothermal treatment and heat-treatment. Fig. 3c and d shows the TEM images of the as-prepared Fe_2O_3 nanotubes. The obvious electron-density differences between the dark edge and pale center further confirm the hollow and tubular structure clearly. As shown in Fig. 3d, the wall thickness for the nanotube is about 10–20 nm. The inserted selective-area electron diffraction pattern indicates the single crystal nature of the Fe_2O_3 nanotubes. Fig. 3e shows a typical HRTEM image that was taken from the open-end region of the single Fe_2O_3 nanotube in Fig. 3d. The lattice spacing about 0.45 nm for (0003) plane of the trigonal Fe_2O_3 [38] can be clearly resolved. Fig. 3f and g shows the TEM images of the Fe_3O_4/carbon core–shell nanotubes. It is clear to see that a thin and continuous carbon layer is coated on the surface of Fe_3O_4 nanotubes. As shown in the inset in Fig. 3g, a magnified TEM image that was taken from the wall of the Fe_3O_4 nanotube indicates carbon coating takes place at both outer side and inner side surfaces of the tube, building a Fe_3O_4/carbon core–shell nanotube heteroarchitecture. The thickness of the carbon layer coated on the Fe_3O_4 nanotubes ranges between 2 and 5 nm. Fig. 3h shows an HRTEM image that was taken from the wall region of the single Fe_3O_4/carbon nanotube in Fig. 3g. The well-resolved lattice fringes with an interplane distance of 0.48 nm come from the (111) plane of Fe_3O_4.

The chemical composition and electronic structure of the Fe_3O_4/carbon core–shell nanotubes were further investigated by XPS. Fig. 4a shows the survey-scan XPS spectrum for the Fe_3O_4/carbon core–shell nanotubes. All obvious peaks are labeled and can be ascribed to Fe, O, and C. Fig. 4b shows the narrow scan XPS spectrum of Fe 2p of the Fe_3O_4/carbon core–shell nanotubes. Two main peaks, located at 710.8 and 724.0 eV, correspond to Fe $2p_{3/2}$ and Fe $2p_{1/2}$, respectively. The Fe $2p_{3/2}$ peak can be best fitted with two components with a major one at 710.6 eV and a minor one at 712.1 eV, which can be ascribed to Fe^{2+} and Fe^{3+}, respectively. Moreover, no shakeup satellite peak situated at ~719 eV, which is
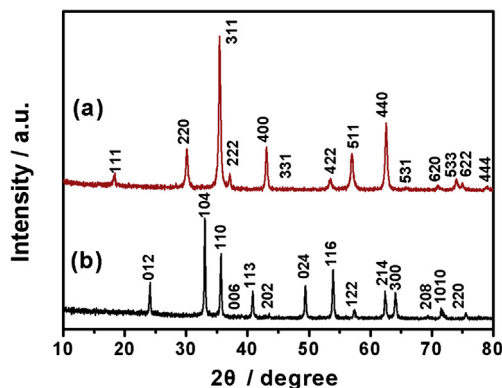

Fig. 1. XRD patterns of (a) the Fe_3O_4/carbon core–shell nanotubes and (b) the α-Fe_2O_3 nanotubes.
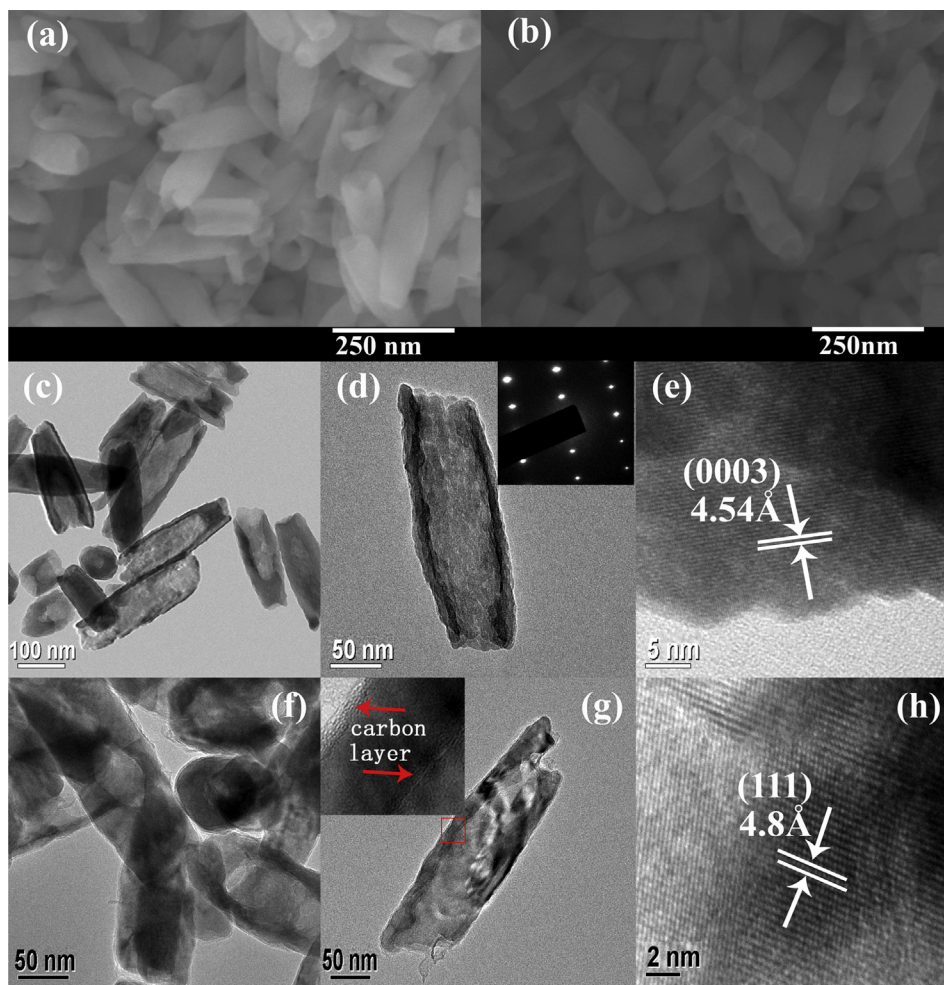
Fig. 3. FESEM images of the Fe_2O_3 nanotubes (a) and the Fe_3O_4/carbon core–shell nanotubes (b). (c, d) TEM images of the Fe_2O_3 nanotubes. (e) HRTEM of a single Fe_2O_3 nanotube. (f, g) TEM images of the Fe_3O_4/carbon core–shell nanotubes. (h) HRTEM of a single Fe_3O_4/carbon core–shell nanotube. Inset in Fig. 3d shows the selective-area electron diffraction pattern of a single Fe_2O_3 nanotube. Inset in Fig. 3g shows the magnified TEM of the wall region of a single Fe_3O_4/carbon core–shell nanotube.

the fingerprint of the electronic structures of Fe_2O_3 [44], confirms no Fe_2O_3 exist in the Fe_3O_4/carbon core–shell nanotubes. As shown in Fig. 4c, the O 1s spectrum is broad and could be deconvoluted into three peaks at 529.9, 531.1, and 533.3 eV, respectively. The peak at 529.9 eV is a typical state of O^{2-} species corresponding to Fe_3O_4, while the rest two peaks could be attributed to the presence of residual oxygen-containing groups (such as –OH and –COOH) bonded with carbon atoms in the carbon layer of the Fe_3O_4/carbon core–shell nanotubes. The C 1s core-level spectrum shown in Fig. 4d can be deconvoluted into three peaks at 284.3, 285.7, and 288.8 eV, respectively. The main peak at 284.3 eV is due to the sp^2-hybridized carbon [45]. The peak at 285.7 eV can be assigned to carbon atoms singly coordinated to an oxygen atom as in phenols or ethers (C–OR) [45]. The small peak at 288.8 eV is attributed to the presence of carbonyl (C=O) groups [45]. ICP was used to quantify the chemical composition of the composite. The results showed that the composites have a chemical composition of 92.8 wt% Fe_3O_4 and 7.2 wt% carbon.

The Fe_3O_4/carbon core–shell nanotube heteroarchitecture could be a promising anode material for LIBs. In the present study, galvanostatic charge/discharge measurements were carried out on the Fe_3O_4/carbon core–shell nanotube electrodes, the pure Fe_3O_4, and the pure Fe_2O_3 nanotube electrodes. Fig. 5a shows the charge/discharge curves of the Fe_2O_3 nanotube electrode at various cycle numbers at a constant current density of 100 mA g^{-1} in the voltage

range between 0.01 and 3.0 V. The first discharge curve of the Fe_2O_3 nanotube electrode exhibits two distinguished voltage plateaus at 1.6 and 0.8 V, respectively, which agrees well with literature reports for the Fe_2O_3 electrodes [24–26]. The first plateau can be ascribed to the formation of cubic $Li_2Fe_2O_3$, and the second plateau can be ascribed to the formation of Fe/Li_2O composite. The first charge curve of the Fe_2O_3 nanotube electrode exhibits a quasi voltage plateau at about 1.6 V, corresponding to the oxidation from Fe^0 to Fe^{3+}. The electrochemical reversible reaction mechanism of lithium storage in Fe_2O_3 during the charge/discharge processes can be described as

$$Fe_2O_3 + 6e^- + 6Li^+ \Leftrightarrow 2Fe^0 + 3Li_2O \qquad (1)$$
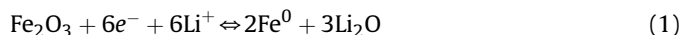
In theory, Fe_2O_3 can have an uptake of 6 Li^+, corresponding to 1005 mAh g^{-1} theoretical specific capacity. It was found that electrochemical lithiation typically leads to formation of nanometer-scale metal clusters embedded in a Li_2O matrix, accompanying a large volume expansion. The high strain associated with the large volume change could lead to the pulverization of the electrode, which induces loss of electrical contact between the electrode material and the current collector, thus resulting in fast capacity fade for the cycling. As shown in Fig. 5b and c, the Fe_3O_4 nanotube electrode and the Fe_3O_4/carbon core–shell nanotube electrode exhibit similar charge/discharge curves. For both electrodes, the first discharge curves (Fig. 5b and c) exhibit only one
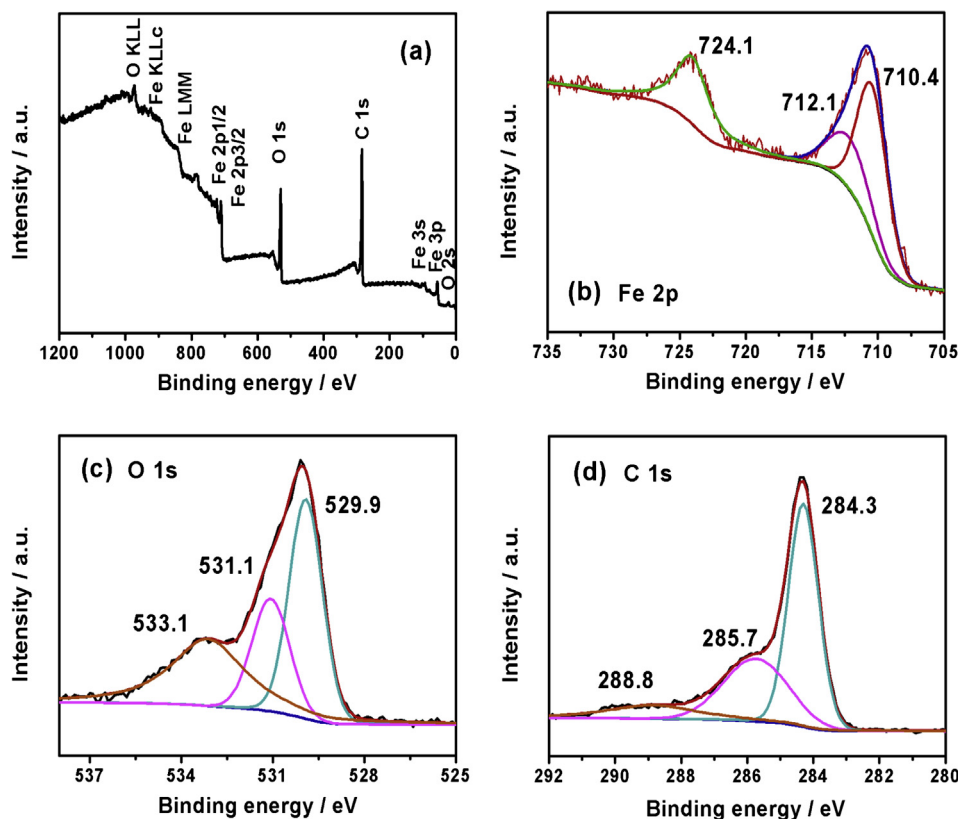
Fig. 4. (a) XPS survey scan spectrum, (b) Fe 2p narrow scan XPS spectrum, (c) O 1s narrow scan XPS spectrum, and (d) C 1s narrow scan XPS spectrum of the Fe_3O_4/carbon core–shell nanotubes.

well-defined plateau at about 0.8 V, corresponding to the reduction of Fe^{3+}/Fe^{2+} to Fe^0, which agrees well with literature reports for the Fe_3O_4 electrodes [26,29]. The electrochemical reversible reaction mechanism of lithium storage in Fe_3O_4 during the charge/discharge processes can be described as

$$Fe_3O_4 + 8e^- + 8Li^+ \Leftrightarrow 3Fe^0 + 4Li_2O \qquad (2)$$
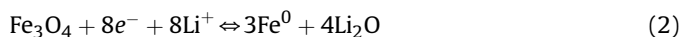
However, Zhang et al. found that Fe_3O_4 was not directly reduced to Fe^0 during the initial discharge process with the formation of an intermediate phase of $Li_xFe_3O_4$ [46,47]. To investigate the inter-mediate reaction, *ex situ* XRD analysis was carried out for the Fe_3O_4/carbon nanotube electrode. Fig. 5d shows the *ex situ* XRD patterns of the Fe_3O_4/carbon nanotube electrode at various discharge states. When the electrode was first discharged to 0.85 V, the diffraction peaks of Fe_3O_4 disappeared while some new peaks appeared. The new diffraction peaks can be attributed to $Li_xFe_3O_4$ [46], which agree well with the previous report, indicating the formation of intermediate phase during the initial discharge process. When the electrode was further discharged to 0.8 V, the diffraction peaks of $Li_xFe_3O_4$ disappeared while a peak ascribed to Li_2O appeared, indicating the intermediate phase was further reduced to Fe^0. When the electrode was discharge to 0.01 V, no diffraction peaks from the electrode material can be observed, which could be ascribed to the nanoparticle nature of the electrochemically formed species. There could be some reasons to explain why XRD cannot detect the $Li_xFe_3O_4$ signals after the first cycle. First, there is an irreversible capacity loss between charge and discharge for the first cycle, which means not all Li inserted during the first discharge can be extracted during the first charge and Fe_3O_4 could not be reformed after the first cycle. For the second discharge, Li is not intercalated into Fe_3O_4 but kind of FeO_x/Li_2O composite, which may

not result in the formation of $Li_xFe_3O_4$ intermediate phase. Second, when the Fe_3O_4 is deeply discharged to 0.01 V and then charged to 3 V, the conversion reaction associated with large volume change could result in the formation of nanocrystallines with nanometer-scale particle size. XRD may not be able to detect such small par-ticles [48]. If Fe_3O_4 can have an uptake of 8 Li^+, a theoretical ca-pacity of 922 mAh g^{-1} could be obtained. The voltage plateau at about 1.6 V for the first charge curve of the Fe_3O_4/carbon core–shell nanotube electrode corresponds to the reversible oxidation of Fe^0 to Fe^{3+}/Fe^{2+}. For the Fe_2O_3 nanotube electrode, the first discharge and charge capacities are 1419 and 1049 mAh g^{-1}, respectively, giving a coulombic efficiency of about 74%. After the first cycle, the charge and discharge are highly reversible with negligible irre-versible capacity. The irreversible capacity loss of the Fe_2O_3 nano-tube electrode for the first cycle is probably due to incomplete conversion reaction and the solid electrolyte interphase layer for-mation at the electrode/electrolyte interface caused by the reduc-tion of electrolyte. Although the charge/discharge capacities of the Fe_2O_3 nanotube electrode fade quickly, the fading rate is much slower compared to the Fe_2O_3 spindles with similar size [26]. The improvement of the cycling stability of the Fe_2O_3 nanotube elec-trode could be attributed to the hollow tubular structure, which can accommodate larger volume changes during the charge/discharge processes. For the Fe_3O_4 nanotube electrode, the first discharge and charge capacities are 1250 and 912 mAh g^{-1}, respectively, giving a coulombic efficiency of about 73%. For the Fe_3O_4/carbon core–shell nanotube electrode, the first discharge and charge capacities are 1213 and 938 mAh g^{-1}, respectively, with a coulombic efficiency of about 77%. It is clear to see that the carbon coating on Fe_3O_4 nanotubes significantly enhances the reversibility of the electrode. As discussed by Guo et al., carbon coating on the Fe_3O_4 particles
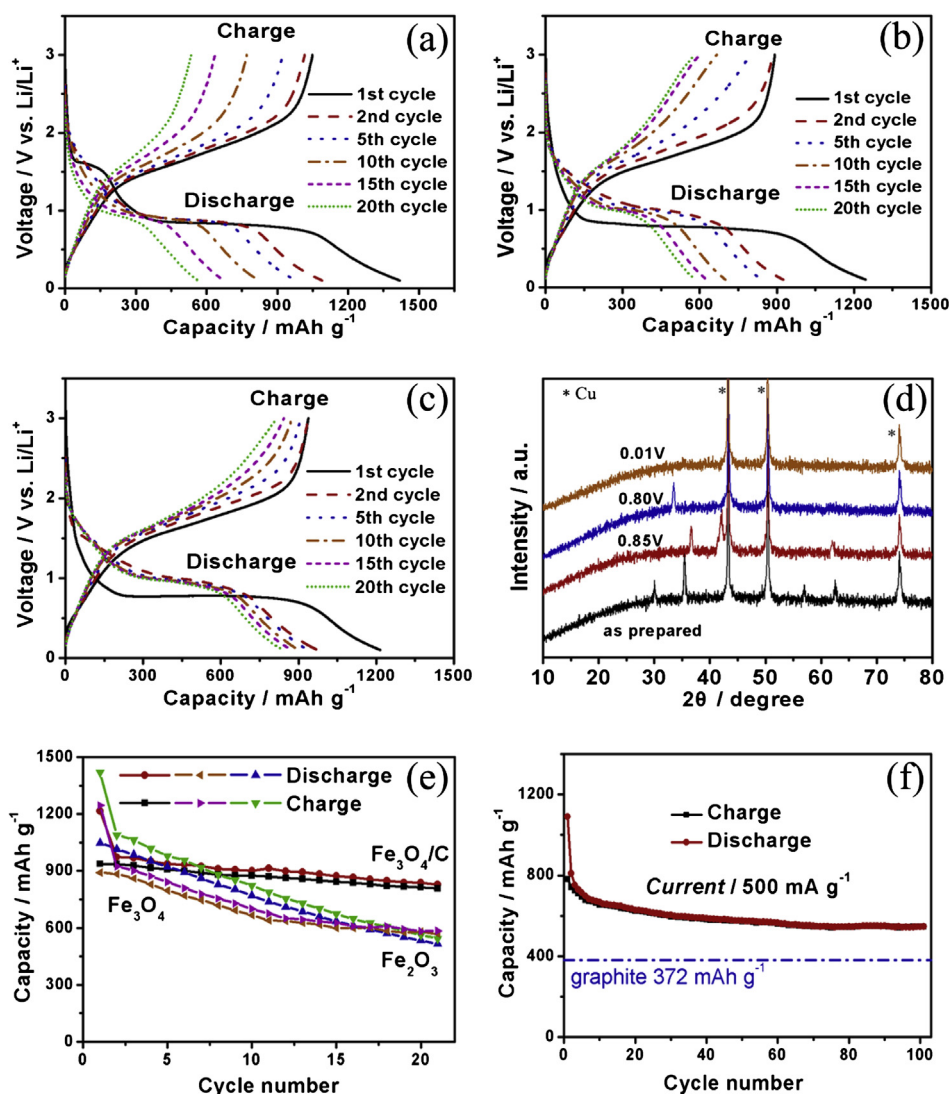
Fig. 5. The charge/discharge curves of (a) the Fe$_2$O$_3$ nanotube electrode, (b) the Fe$_3$O$_4$ nanotube electrode, and (c) the Fe$_3$O$_4$/carbon core–shell nanotube electrode at a current density of 100 mA g^{-1}. (d) *ex situ* XRD patterns of the Fe$_3$O$_4$/carbon nanotube electrode at various discharge states. (e) Cycle performance of the Fe$_2$O$_3$ nanotube electrode, the Fe$_3$O$_4$ nanotube electrode, and the Fe$_3$O$_4$/carbon core–shell nanotube electrode at a current density of 100 mA g^{-1} for 20 cycles. (f) Cycle performance of the Fe$_3$O$_4$/carbon core–shell nanotube electrode at a current density of 500 mA g^{-1} for 100 cycles.

could not only suppress the formation of SEI films but also stabilize the formed SEI films, thus leading to an improved initial coulombic efficiency and better cycling stability [26]. In addition to the formation of the SEI layer, the irreversible capacity for the first cycle is highly dependent on the mobility of Li$^+$ and e^- during Li extraction process. The uniformly coated carbon layer on the surface of Fe$_3$O$_4$ nanotubes can greatly improve the electrical conductivity of the electrode. As discussed by Li et al., Li extraction reaction stops at a depth where the carriers cannot be sufficiently transported through the metal oxide phase in the time scale of the experiment [49]. Li$^+$ and e^- transport could be greatly enhanced as the particle size is reduced from micrometer to nanometer. A hollow tube nanostructure could further enhance the reversible capacity of the electrode as the Li$^+$ and e^- diffusion paths can be further reduced due to the thin tube walls. As a result, the first reversible capacity of the Fe$_3$O$_4$/carbon core–shell nanotubes is much larger than that of the Fe$_3$O$_4$/carbon nanospindles with similar particle size (749 mAh g^{-1}) [26]. Fig. 5e shows the charge/discharge cycle performance of the Fe$_2$O$_3$ nanotube, the Fe$_3$O$_4$ nanotube, and the Fe$_3$O$_4$/carbon core–shell nanotube electrodes at a current density

of 100 mA g^{-1} for 20 cycles. It is obvious that the Fe$_3$O$_4$/carbon core–shell nanotube electrode exhibits much better cyclability compared to both the Fe$_2$O$_3$ and Fe$_3$O$_4$ nanotube electrodes. After 20 cycles, the Fe$_3$O$_4$/carbon core–shell nanotube electrode can deliver a reversible capacity of 808 mAh g^{-1}, corresponding to 86% capacity retention of the initial reversible capacity. By contrast, the reversible capacities of the Fe$_2$O$_3$ nanotube and Fe$_3$O$_4$ nanotube electrodes are only 534 mAh g^{-1} and 591 mAh g^{-1}, respectively, after 20 cycles. The corresponding capacity retentions of the initial reversible capacities for the Fe$_2$O$_3$ and Fe$_3$O$_4$ nanotube electrodes are 53% and 65%, respectively. The superior cycling stability of the Fe$_3$O$_4$/carbon core–shell nanotube electrode can be attributed to the carbon coating. The coated carbon layer formed a shell that tightly attached to the Fe$_3$O$_4$ nanotube, which not only improved the electrical conductivity of the electrode but also greatly enhanced the structural stability. The carbon shell can work as a buffer layer that can effectively suppresses the volume change of Fe$_3$O$_4$ and reduces the loss of electrical contact of the pulverized Fe$_3$O$_4$ particles during the cycling, thus leading to greatly improved cycling stability. The cycle performance of the Fe$_3$O$_4$/carbon core–

shell nanotube electrode was further investigated by charge/discharge measurements at a current density of 500 mA g^{-1} for 100 cycles. As shown in Fig. 5d, the Fe$_3$O$_4$/carbon core–shell nanotube electrode retains 70% of its initial reversible capacity after 100 cycles. The cycling stability of the Fe$_3$O$_4$/carbon core–shell nanotube electrode is greatly improved compared with that of the Fe$_3$O$_4$/carbon core–shell nanorod electrode reported by Liu and Wang et al. [28]. It can be seen that the capacity decay of the Fe$_3$O$_4$/carbon core–shell nanotube electrode after 60 cycles is almost negligible. After 100 cycles, the Fe$_3$O$_4$/carbon core–shell nanotube electrode can still deliver a reversible capacity of 560 mAh g^{-1}, which is much higher than the theoretical capacity of the commercial graphite electrode.

In addition to the greatly improved cycle performance, the Fe$_3$O$_4$/carbon core–shell nanotube electrode also exhibits excellent rate capability as demonstrated in Fig. 6. To perform the rate capability measurements, the electrode was charged and discharged for 5 cycles at different current densities from 100 to 2000 mA g^{-1}. Fig. 6a shows the second charge/discharge curves of the Fe$_3$O$_4$/carbon core–shell nanotube electrode at different current densities. It is noticed that the cell polarization increases with decreasing reversible capacity as the current density increases. Fig. 6b shows the specific charge/discharge capacities of the Fe$_3$O$_4$/carbon core–shell nanotube electrode as a function of cycle number at different current densities. The reversible capacity of the Fe$_3$O$_4$/carbon core–shell nanotube electrode drops from 932 to

470 mAh g^{-1} when the current density increases from 100 to 2000 mA g^{-1}. Even at a high current density of 2000 mA g^{-1}, the Fe$_3$O$_4$/carbon core–shell nanotube electrode still can deliver a reversible capacity much higher than the theoretical capacity of graphite (372 mAh g^{-1}). The rate capability of the Fe$_3$O$_4$/carbon core–shell nanotube electrode in the present study is much better than that of the Fe$_2$O$_3$ nanorod arrays [12], carbon coated Fe$_3$O$_4$ dendrites [30], and Fe$_3$O$_4$/carbon nanospindles [26] as reported in literature. The superior rate capability of the Fe$_3$O$_4$/carbon core–shell nanotube electrode could be attributed to its hollow tubular structure and continuous carbon coating. The hollow tubular structure shortens the Li$^+$ ion diffusion path through the thin tube walls, and the continuous carbon coating on the surface of Fe$_3$O$_4$ nanotubes enhances the electronic conductivity of the electrode, thus leading to fast charge transport in the electrode.

4. Conclusions

Fe$_3$O$_4$/carbon core–shell nanotubes were successfully prepared by a simple chemical route without using of template. The Fe$_3$O$_4$/carbon core–shell nanotube electrode exhibits a large reversible capacity up to 938 mAh g^{-1} and a high initial coulombic efficiency of 77%. The improved initial coulombic efficiency of the Fe$_3$O$_4$/carbon core–shell nanotube could be attributed to its continuous carbon coating, which could suppress and stabilize the SEI layer formation. The Fe$_3$O$_4$/carbon core–shell nanotube electrode also exhibits greatly improved cycle performance compared to the Fe$_2$O$_3$ nanotube electrode and excellent rate capability, making it promising as anode material for the next-generation high performance LIBs. The superior electrochemical performance of the Fe$_3$O$_4$/carbon core–shell nanotube electrode can be attributed to its hollow tubular structure and continuous carbon coating, which favor large volume changes and fast charge transport.

Fig. 6. (a) The charge/discharge curves of the Fe$_3$O$_4$/carbon core–shell nanotube electrode at different current densities. (b) Charge/discharge capacities of the Fe$_3$O$_4$/carbon core–shell nanotube electrode as a function of cycle number at different current densities.

References

[1] J.M. Tarascon, M. Armand, Nature 414 (2001) 359–367.
[2] L. Shen, C. Yuan, H. Luo, X. Zhang, K. Xu, Y.Y. Xia, J. Mater. Chem. 20 (2010) 6998–7004.
[3] S. Hariharan, K. Saravanan, P. Balaya, Electrochem. Solid-State Lett. 13 (2010) A132–A135.
[4] Y. Chen, H. Xia, L. Lu, J.M. Xie, J. Mater. Chem. 22 (2012) 5006–5012.
[5] X.H. Huang, J.P. Tu, X.H. Xia, X.L. Wang, J.Y. Xiang, Electrochem. Commun. 10 (2008) 1288–1290.
[6] Y. Wang, H.J. Zhang, L. Lu, L.P. Stubbs, C.C. Wong, J.Y. Lin, ACS Nano 4 (2010) 4753–4761.
[7] J.M. Kim, Y.S. Huh, Y.K. Han, M.S. Cho, H.J. Kim, Electrochem. Commun. 14 (2012) 32–35.
[8] M.V. Reddy, T. Yu, C.H. Sow, Z.X. Shen, C.T. Lim, G.V. Subba Rao, B.V.R. Chowdari, Adv. Funct. Mater. 17 (2007) 2792–2799.
[9] B. Wang, J.S. Chen, H.B. Wu, Z.Y. Wang, X.W. Lou, J. Am. Chem. Soc. 133 (2011) 17146–17148.
[10] J.S. Chen, T. Zhu, C.M. Li, X.W. Lou, Angew. Chem. Int. Ed. 50 (2011) 650–653.
[11] Z.Y. Wang, L. Zhou, X.W. Lou, Adv. Mater. 24 (2012) 1903–1911.
[12] Z.S. Hong, T.B. Lan, F.Y. Xiao, H.X. Zhang, M.D. Wei, Funct. Mater. Lett. 4 (2011) 389–394.
[13] Z.S. Hong, T.B. Lan, Y.Z. Zheng, L.L. Jiang, M.D. Wei, Funct. Mater. Lett. 4 (2011) 65–70.
[14] G.B. Cho, K.W. Kim, T.Y. Nam, Funct. Mater. Lett. 2 (2009) 37–40.
[15] Y.Q. Song, S.S. Qin, Y.W. Zhang, W.Q. Gao, J.P. Liu, J. Phys. Chem. C 114 (2010) 21158–21164.
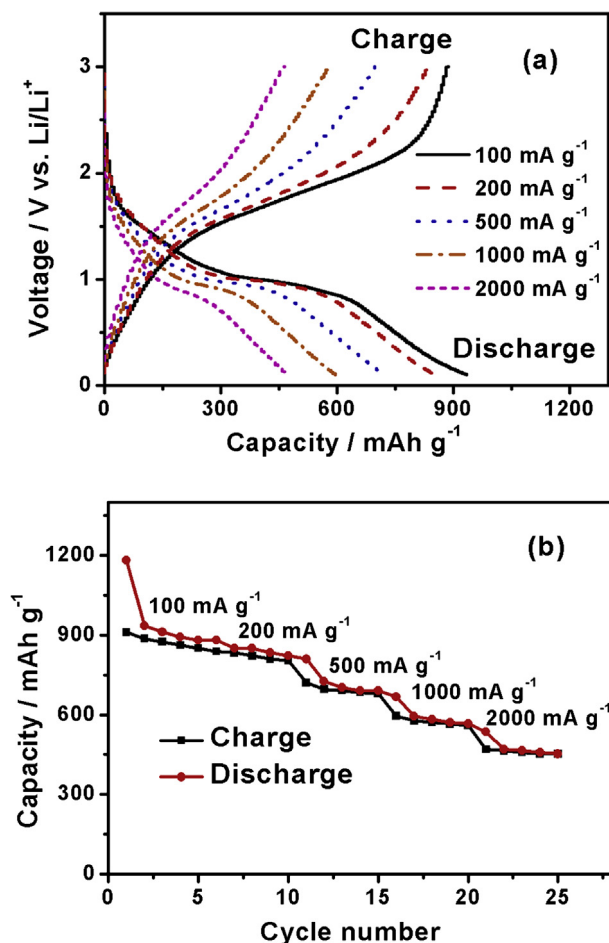[16] P.L. Taberna, S. Mitra, P. Poizotm, P. Simon, J.M. Tarascon, Nat. Mater. 5 (2006) 567–573.

[17] W.F. Chen, S.R. Li, C.H. Chen, L.F. Yan, Adv. Mater. 23 (2011) 5679−5683.
[18] T. Muraliganth, A.V. Murugan, A. Manthiram, Chem. Commun. 47 (2009) 7360−7362.
[19] L.H. Duan, Y.D. Huang, D.Z. Jia, X.C. Wang, Z.P. Guo, Mater. Lett. 71 (2012) 151−153.
[20] W.D. Zhang, X.Y. Wang, H.H. Zhou, J.T. Chen, X.X. Zhang, J. Alloys Compd. 521 (2012) 39−44.
[21] K.Y. Xie, Z.G. Lu, H.T. Huang, W. Lu, Y.Q. Lai, J. Li, L.M. Zhou, Y.X. Liu, J. Mater. Chem. 22 (2012) 5560−5567.
[22] C.J. Jia, L.D. Sun, Z.G. Yan, L.P. You, F. Luo, X.D. Han, Y.C. Pang, Z. Zhang, C.H. Yan, Angew. Chem. Int. Ed. 44 (2005) 4328−4333.
[23] C.J. Jia, L.D. Sun, F. Luo, X.D. Han, Laura J. Heyderman, Z.G. Yan, C.H. Yan, K. Zheng, Z. Zhang, M. Takano, N. Hayashi, M. Eltschka, M. Klaui, U. Rudiger, T. Kasama, L. Cervera-Gontard, Rafal E. Dunin-Borkowski, G. Tzvetkov, J. Raabe, J. Am. Chem. Soc. 130 (2008) 16968−16977.
[24] J.P. Liu, Y.Y. Li, H.J. Fan, Z.H. Zhu, J. Jiang, R.M. Ding, Y.Y. Hu, X.T. Huang, Chem. Mater. 22 (2010) 212−217.
[25] Z.Y. Wang, D.Y. Luan, S. Madhavi, C.M. Li, X.W. Lou, Chem. Commun. 47 (2011) 8061−8063.
[26] W.M. Zhang, X.L. Wu, J.S. Hu, Y.G. Guo, L.J. Wan, Adv. Funct. Mater. 18 (2008) 3941−3946.
[27] S.L. Jin, H.G. Deng, D.H. Long, X.J. Liu, L.A. Zhan, X.Y. Liang, W.M. Qiao, L.C. Ling, J. Power Sources 196 (2011) 3887−3893.
[28] H. Liu, G.X. Wang, J.Z. Wang, D. Wexler, Electrochem. Commun. 10 (2008) 1879−1882.
[29] Y.Z. Piao, H.S. Kim, Y.E. Sung, T. Hyeon, Chem. Commun. 46 (2010) 118−120.
[30] M. Zhang, X.M. Yin, Z.F. Du, S.A. Liu, L.B. Chen, Q.H. Li, H. Jin, K. Peng, T.H. Wang, Solid State Sci. 12 (2010) 2024−2029.
[31] Y. Ma, G. Ji, J.Y. Lee, J. Mater. Chem. 21 (2011) 13009−13014.

[32] S.M. Yuan, Z. Zhou, G. Li, CrystEngComm 13 (2011) 4709−4713.
[33] T. Zhu, J.S. Chen, X.W. Lou, J. Phys. Chem. C 115 (2011) 9814−9820.
[34] F. Cheng, K.L. Huang, S.Q. Liu, J.L. Liu, R. Deng, J. Electrochim. Acta 56 (2011) 5593−5598.
[35] Z.Y. Wang, D.Y. Luan, S. Madhavi, Y. Hu, X.W. Lou, Energy Environ. Sci. 5 (2012) 5252−5256.
[36] Y.D. Huang, Z.F. Dong, D.Z. Jia, Z.P. Guo, W.I. Cho, Electrochim. Acta 56 (2011) 9233−9239.
[37] Y. Ma, C. Zhang, G. Ji, J.Y. Lee, J. Mater. Chem. 22 (2012) 7845−7850.
[38] H.M. Fan, G.J. You, Y. Li, Z. Zheng, H.R. Tan, Z.X. Shen, S.H. Tang, Y.P. Feng, J. Phys. Chem. C 113 (2009) 9928−9935.
[39] H.M. Fan, J.B. Yi, Y. Yang, K.W. Kho, H.R. Tan, Z.X. Sen, J. Ding, X.W. Sun, M.C. Olivo, Y.P. Feng, ACS Nano 3 (2009) 2798−2808.
[40] D.L.A. de Faria, S. Venancio Silva, M.T. De Oliveira, J. Raman Spectrosc. 28 (2007) 873−878.
[41] F. Tuinstra, J.L. Koening, J. Chem. Phys. 53 (1970) 1126−1130.
[42] P.C. Eklund, J.M. Holden, R.A. Jishi, Carbon 33 (1995) 959−972.
[43] Y.J. Chen, G. Xiao, T.S. Wang, Q.Y. Ouyang, L.H. Qi, Y. Ma, P. Gao, C.L. Zhu, M.S. Cao, H.B. Jin, J. Phys. Chem. C 115 (2011) 13603−13608.
[44] T. Fujii, F.M.F. de Groot, G.A. Sawatzky, Phys. Rev. B 59 (1999) 3195−3202.
[45] J.F. Moulder, W.F. Stickle, P.E. Sobol, K.D. Bomben, Handbook of X-ray Photoelectron Spectroscopy, Perkin Elmer Corp., Minnesota, 1992.
[46] Q.M. Zhang, Z.C. Shi, Y.F. Deng, J. Zheng, G.C. Liu, G.H. Chen, J. Power Sources 197 (2012) 305−309.
[47] S.Q. Wang, J.Y. Zhang, C.H. Chen, J. Power Sources 195 (2010) 5379−5381.
[48] P. Poizot, S. Laruelle, S. Grugeon, L. Dupont, J.M. Tarascon, Nature 407 (2000) 496−499.
[49] H. Li, P. Balaya, J. Maier, J. Electrochem. Soc. 151 (2004) A1878−A1885.